Journal of Materials Research and Technology 33 (2024) 6820–6830

Contents lists available at ScienceDirect

Journal of Materials Research and Technology

journal homepage: www.elsevier.com/locate/jmrt

Co-extrusion of highly loaded feedstocks for fabrication of stainless steel-bioceramic core-shell structures

Lisa Biasetto *, Vanessa Gastaldi, Hamada Elsayed

Department of Industrial Engineering, University of Padova, via Marzolo 9, 35131, Padova, Italy

ARTICLE INFO

Handling editor: P.Y. Chen

Keywords:
Direct ink writing
Co-extrusion
Core-shell
Steel 316L
Sphene bioceramics

ABSTRACT

Co-extrusion of multi-materials structures shows technological challenges and opportunities. Filaments made of a metallic core and a ceramic shell are one example of how structural and functional features can be combined in a single component to provide a synergic effect. In this work, we focused on the fabrication of shell and core-shell scaffolds for potential applications as bone substitutes. Stainless steel 316L was selected for the core material, whilst in situ synthesized sphene ($CaTiSiO_5$) bioactive ceramic was selected as a shell. The combination of a ductile core and a bioactive ceramic, so as scaffolds made of empty struts may represent a new generation of bone substitutes with mechanical properties closer to the ones of natural bone so as with improved bioactivity. Therefore, formulated inks were co-extruded in one step using a customized printing set-up. Microstructural and mechanical properties were investigated on shell and core-shell filaments and 3D structures. Shell bioceramics scaffolds possessed high porosity and target compression strength values. The sintering environment at the core-shell interface caused severe 316L oxidation thus compromising the ductility of the metallic part, however compression strength increased of 53% compared to shell structures.

1. Introduction

Room temperature co-extrusion of inks through Direct Ink Writing (DIW) is sprouting as a game changing technology: it can potentially impact multiple sectors such as biomedical, aerospace, automotive, electronics, and thermal energy industries, but it shows several challenges in terms of inks formulation, printing process, de-binding and sintering, particularly, when ceramics and/or metals are used.

The combination of materials with complementary properties is a well-known concept in composites, where materials are combined to get a synergic effect. Nevertheless, there are several forthcoming advancements that DIW co-extrusion offers: for instance, diverse materials can be combined in the configuration of a long-aligned fiber until now limited to polymeric matrix composites reinforced with carbon, SiC, or glass fibers, so as metals and ceramics can be merged to build intricate 3D structures. The above advantages will converge toward the fabrication of components with tunable structural and functional properties operating in a range of unprecedented service conditions.

Examples of co-extrusion by DIW are the ones with cross linkable polymeric inks used to show how composition (flexible core and brittle shell) and process parameters can affect the mechanical properties of the produced parts [1]. Other examples of co-extrusion of polymer-based inks have the primary objective to show the possibility of 3D printing structures with functional properties, such as bio-scaffolds [2], lithium iron phosphate batteries [3] and low temperature thermal energy storage systems [4]. In a more challenging way to dig the co-extrusion DIW, other researchers focus on the formulation of ceramic-based inks. In this case, ink formulation must pass through the control of printing parameters so as the de-binding and sintering steps. Examples of tested compositions are C- Al_2O_3 [5,6], C_f-SiC [7], indium tin oxide-Al_2O_3 [8], Al_2O_3 with graphene nanoplatelets and Al_2O_3 [9], where both mechanical [5,7] and functional properties are investigated [8,9].

Due to the further degree of complexity deriving from metal and ceramic co-sintering, only one example of co-extrusion of steel- Al_2O_3 can be found in the literature where the improvement of mechanical strength and toughness are demonstrated [10].

On the basis of available literature data [1–10], the co-extrusion DIW technology can be classified into two main categories: the single step and the multi-step process. The single step process can find various interpretations: “the syringe in a syringe”, where a small syringe is contained inside a larger one and the two immiscible inks flow through a single nozzle [2]; “the co-extrusion nozzle” where the two inks flow in

* Corresponding author.
E-mail address: lisa.biasetto@unipd.it (L. Biasetto).

https://doi.org/10.1016/j.jmrt.2024.10.255
Received 9 September 2024; Received in revised form 28 October 2024; Accepted 30 October 2024
Available online 8 November 2024

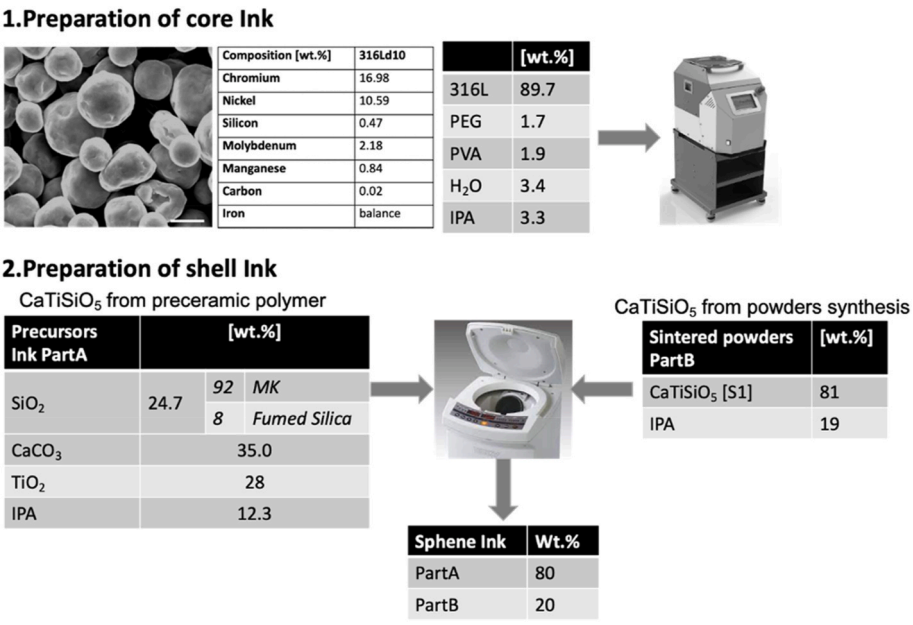

Fig. 1. Core ink preparation includes morphology and composition of 316L gas atomized particles (scale bar is 5 μm), as well as 316L ink formulation and mixing (a). Preparation of shell ink, composition (PartA and PartB) mixing, and weight ratio details (b).

separate channels and through two concentric nozzles [5]. The multi-step process can also find various interpretations: sacrificial core and post-printing infiltration [7], molding of the shell inside the syringe and core-shell co-extrusion through a single nozzle [10].

Beyond the various facets, common points arise when approaching DIW co-extrusion: inks and the co-extrusion set-up must grant for a continuous flow without clogging and a self-sustainable printed shape. In this regard, inks' rheological properties play the main role: inks must be formulated to maximize the amount of solid load so as to grant for non-Newtonian Hershchel and Bulkley fluid behaviour [11,12]. The nozzle shape must be optimized to minimize wall friction and grant for continuous flow at low pressures ($P < 8 \times 10^5$ Pa).

In addition, when ceramics and metals are used, the de-binding and sintering process must not compromise the structural integrity of the part due to thermal stress and/or unwanted reaction byproducts that may be generated during sintering. Thermally induced stress depends on the coefficient of thermal expansion, Young and Poisson Modules that must be tuned to avoid fracture. The study of thermally induced stress in core-shell structures is limited to the case of spherical shapes and composites with particles reinforcement [13,14,15], whilst literature is lacking the modelling of a cylindrical core-shell configuration.

Following [13], the residual radial stress in a core-shell configuration can be expressed by the following formula:

$$\sigma_R = \frac{\Delta\alpha\Delta T}{\frac{1-2\upsilon_1}{E_1} - \frac{1+\nu_2}{2E_2}} \quad \text{(Eq.1)}$$

where $\Delta\alpha = \alpha_1 - \alpha_2$ (with α the coefficient of thermal expansion in K^{-1} of core and shell respectively) $\Delta T = T_f - T_0$ is the temperature difference upon heating and/or cooling, E and ν are the Young (Pa) and Poisson (−) moduli of the core and shell materials. During the dwelling of sintering process $T_f = T_0$ and ΔT is equal to zero, but stresses arise during the heating and cooling stages. Strategies to control thermally induced stresses with a selected combination of materials may consist of tuning CTE by ink formulation and solid load, so as by tuning the values of E and ν controlling residual porosity [6].

The primary aim of this study is to illustrate the viability of employing a one-step co-extrusion method where steel-bioceramics core-shell 3D structures are fabricated by a reactive sintering process. PLA-Hydroxyapatite core-shell 3D structures were fabricated by a two steps process in Ref. [7] showing how mechanical strength and strain energy density were compatible with the ones of natural bone.

Here, we propose using stainless steel 316L as the core material and sphene bioceramic (titanite, $CaTiSiO_5$) as the shell material, which has demonstrated improved bioactivity compared to standard bioceramics [16]. In our previous studies, sphene was successfully synthesized and printed as 3D scaffolds, which were then assessed in vitro and in vivo [17,18]. Stainless steel 316L [19] and titanium Ti6Al4V [20] were also printed and sintered using DIW. In the current study, 316L as a core material is used to improve mechanical properties compared to the ones of sphene shell 3D structures. The main challenges associated with the present study are the control of the printing process as well as the sintering step, where sphene bioceramics were synthesized in situ using the polymer-derived ceramics route [21].

2. Experimental part

2.1. Inks preparation

2.1.1. 316L ink

The 316L ink was formulated following the procedure previously described [22]. In particular, 316L gas atomized powders, with $d_{10} < 5.2$ μm; $d_{50} < 7.1$ μm; $d_{90} < 10.1$ μm were purchased from Eckart TLS GmbH. Powder composition and morphology are represented in Fig. 1a. First, distilled water and isopropyl alcohol (IPA) were mixed in a weight ratio of 50/50 and then used to solve Polyvinyl alcohol (PVA, Sigma-Aldrich Mw = 9000–10.000 $gmol^{-1}$, 80% hydrolized) and Polyethylene glycol (PEG Sigma Aldrich Mn = 950-1000 $gmol^{-1}$), with the following weight ratio: PVA:PEG: (H_2O + IPA) = 18.75:16.25: 65, to act as a binder. Afterward, 316L powders and binder were mixed with the volume ratio (V_{powder}/V_{binder}): VR = 1.07, using a vacuum centrifugal mixer (Hauschild speedmixer) with the following cycle: 2 min 1000 rpm, 1.5 min vacuum ($P = 10^3$ Pa), 20 s vacuum at 1000 rpm (Fig. 1). The use of both distilled water and IPA as solvent material for polymeric binders was driven by the need to control the rate of solvents evaporation after printing in core and shell parts [Fig. S4].

2.1.2. Sphene ink

$CaTiSiO_5$-based ink was prepared by mixing ink PartA, made of precursors dissolved in IPA, and ink PartB made of synthesized sphene

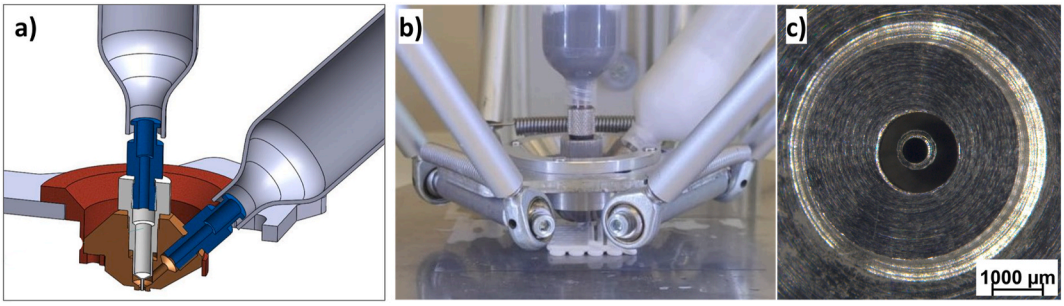

Fig. 2. a) Co-extrusion nozzle design; b) real components; c) detail of core and shell diameters.

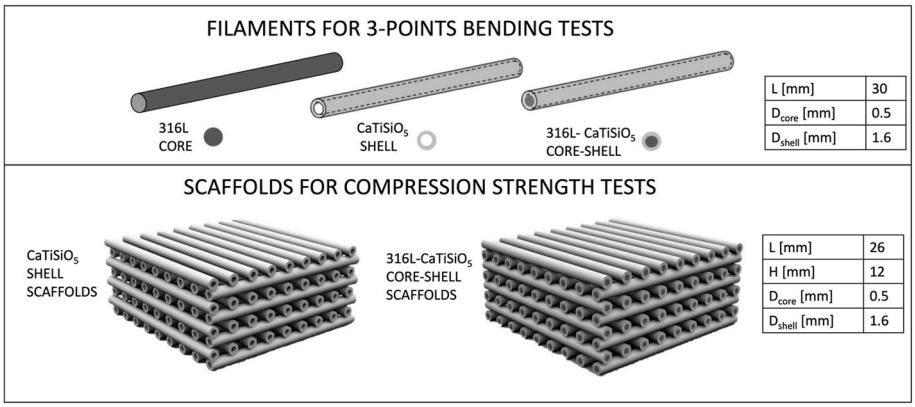

Fig. 3. Designed geometries for 3D-printed filaments and scaffolds.

powders dispersed in IPA (Fig. S1). The scheme of the ink preparation is shown in Fig. 2b. The precursors dispersion (PartA in Fig. 2b) was prepared following the preceramic polymer route as previously reported [17]. Briefly, polymethilsiloxane was used as SiO_2 source (MK Wacker Chemie), fumed silica (R805) was used as SiO_2 source and thickener, TiO_2 (Inframat Advanced Materials, Anatase Nanopowder) and $CaCO_3$ (Bitossi, calcium carbonate micropowders) were used as received. Powders were added gradually and gently blended into IPA. After adding all the solids, the mixture was processed in a Thinky mixer with the following conditions: mixing for 3 min at 2000 rpm. The weight amount of precursors was defined keeping a 1:1:1 = SiO_2:CaO:TiO_2 molar ratio [S1], considering the MK ceramic yield of 84 wt%. Ink PartB was prepared by adding synthetized sphene powder [S1] to IPA with the following weight ratio, IPA: synthetized sphene = 19:81. The mixture was then mixed in a Thinky mixer for 2 min at 2000 rpm.

PartA and PartB of the ink were then mixed in 80 to 20 wt percentage in a Thinky mixer with the following conditions: mixing 3 min at 2000 rpm and defoaming 2 min at 1000 rpm. The 20 wt% amount of ink PartB is the outcome of the shrinkage, printability and drying investigation testified in [S2].

2.2. Rheological characterization of the inks

Rheological properties were measured at room temperature (T = 25 °C) to quantify the physical properties affecting the produced inks' printability. A plate-plate rheometer (d = 40 mm, Netzsch, Kinexus) with solvent trap under IPA was used. Large amplitude oscillatory shear stress (LAOStress) measurements [23] were performed at controlled shear stress in the range of 1–1000 Pa or 1–10000 Pa, at 0.5 Hz with a 0.4 mm gap. The log–log plot of complex viscosity versus shear stress was used to define the rheological behavior of the inks. By mean of storage modulus G′ and loss modulus G″ versus shear stress log–log plots, the following parameters were determined [24]: the linear viscoelastic region (LVR), the stress at the crossover point s_f where G' = G″, and the stress at the yield point s_y (G' = 0.95 G'LVR). The crossover point defines the step over which the viscous behavior overcomes the elastic behavior, meaning that the acting shear stress partially destroys the ink's structure. The thixotropic properties of the inks were assessed utilizing a three-step recovery test at controlled shear stress: a stress, of 0.1 and 100 Pa, was applied for 30 s, and then the viscosity recovery was monitored with a stress of 0.1 Pa for 600 s.

2.3. Co-extrusion of the inks

The co-extrusion was performed using a WASP 2040 Clay (WASP, Massa Lombarda-Ravenna, Italy) equipped with a customized co-extrusion nozzle (Fig. 3). Flow was achieved by applying pressure in the range of 1–5 (x10^5 Pa). The nozzle was designed with conical geometry to favor the flow of the pseudoplastic inks through both the core and shell cavities. It should be noted that the pressure-driven flow of Newtonian fluids is governed by the Hagen Poiseulle law (Eq. (2)) and the wall friction only influences the volumetric flow in the very first layers near to the wall. For non-Newtonian and more specifically for pseudoplastic Herschel and Bulkley fluids, the wall friction affects a thicker layer of fluid (modified Hagen-Poiseulle law, Eq. (3)) [25].

$$Q = \frac{\pi R^3}{\frac{1}{n}+3}\left(\frac{\Delta P}{L}\frac{R}{2k}\right)^{\frac{1}{n}} \quad \text{(Eq.3)}$$

$$Q = \frac{\Delta P \pi R^4}{8\eta L} \quad \text{(Eq.2)}$$

where Q is the volumetric flow in mm^3/s, R is the nozzle diameter, DP is the pressure drop in Pa, h is the Newtonian viscosity in Pa·s, L is the nozzle length, k is the consistency index [Pa·s^n], and n is the power law exponent. For narrow geometries, as is the case of this study (d_{core} = 500 μm d_{shell} = 1600 μm $shell_{thickness}$ = 400 μm) the wall friction will affect a wide fraction of filament thickness thus hindering the inks' flow.

Table 1
Printing parameters for filaments and 3D scaffolds.

Printing parameters		Printed geometries						
		316L Full filament	$CaTiSiO_5$ Full filament	$CaTiSiO_5$ Shell filament	316L- $CaTiSiO_5$ Core-shell filament	316L_PEI-$CaTiSiO_5$ Core-shell filament	$CaTiSiO_5$ Shell scaffolds	316L- $CaTiSiO_5$ Core-shell scaffolds
Pressure [x10^5 Pa]	Core	2–2.5	4	–	5	3 4 5	–	5
	Shell	–	–	4–4.5	4–4.5	4–4.5	4–4.5	4–4.5
F [mm/min]		–	–	–	–	–	600	600
Spacing distance (x-y) [mm]		–	–	–	–	–	3	3
Interlayer distance (z) [mm]		–	–	–	–	–	1.5	1.5

Different geometries were printed, full filaments, shell filaments, core-shell filaments, 3D shell scaffolds and 3D core-shell scaffolds (Fig. 3): 316L dense filaments (conical nozzle, D_{nozzle} = 1600 μm), sphene shell filaments (outer diameter Do_{nozzle} = 1600 μm and inner diameter Di_{nozzle} = 800 μm) and 316L-sphene core-shell filaments (Do_{nozzle} = 1600 μm Di_{nozzle} = 800 μm, D_{core} = 500 μm) of at least 30 mm length (L) were produced to test the flexural strength. Sphene shell scaffolds and 316L-sphene core-shell scaffolds with nominal dimensions of 26 mm length, 26 mm width and 12 mm thickness were produced for compression tests. The scaffolds geometry corresponded to a 4-layers shape with 0°/90° layers orientation.

Filaments were vertically extruded with an applied pressure of 2–2.5 (x10^5 Pa) and cut after the designed length was reached. The vertical extrusion of the filaments was chosen to avoid shape deformation caused by filament-plate adhesion.

The open-source Fullcontrol-Gcode software [26] was used to optimize printing parameters in terms of layer height and printing speed for 3D scaffolds. Pressure was used to extrude the inks and was set to the following values: P_{shell} = 4 (x10^5 Pa), P_{core} = 5 (x10^5 Pa).

To optimize core-shell size tunability, increase the 316L core thickness, and eventually reduce the shell thickness, the 316L ink was modified using 1 wt% of Polyethilenimmine (PEI) on the amount of 316L powders. PEI acts as a surfactant reducing particle-particle interaction and, as a result, ink viscosity, G′, and G″, as well as the flow point of the ink. Rheological investigations were also done on the ink 316L_PEI as described in section 2.2.

Filaments were printed keeping the printing pressure for the sphene-based ink constant at P_{shell} = 4–4.5 (x10^5 Pa) whilst pressure was varied from 3 (x10^5 Pa) to 4 (x10^5 Pa) and 5 (x10^5 Pa) respectively for the 316L based ink (Table 1). The effect of pressure on core and shell size was quantified by measuring the ratio of core area over the total area of the filament. Images of the transversal section of the printed filaments were acquired by stereomicroscopy (AxioCamERc 5s Microscope Camera, Carl Zeiss Microscopy, US), and processed by ImageJ open-source software.

After printing, all samples were dried overnight at room conditions. After drying, samples were placed in static air at 80 °C for 2 h, to crosslink the polysiloxane component of the sphene precursors ink.

2.4. De-binding and sintering

TGA-DTA analyses (TGA-differential scanning calorimetry 3 star System, Mettler Toledo) were performed under an argon atmosphere with a heating rate of 5 °C/min up to 1400 °C. Sintering was performed under an argon atmosphere with the following cycle: 1 °C/min up to 550 °C with a dwell time 1 h for binder removal, 1 °C/min up to 1240 °C dwell time 1 h. The furnace was left to cool down statically. The proposed thermal cycle is based on past experience with 316L de-binding and sintering [27].

2.5. Microstructural and mechanical characterization

Geometrical characterization was carried out using a stereo optical microscope (AxioCamERc 5s Microscope Camera, Carl Zeiss Microscopy, US), the software ImageJ was used to assess core and shell size, the core area percentage was quantified as (A_{core}/A_{tot})% with A_{tot} = A_{core} + A_{shell}. The size of the scaffolds, after printing and after sintering, was also measured by a digital calliper, from which values of linear and volumetric shrinkage were determined, so as these measurements were used to calculate the scaffolds' geometric porosity, using the following formula:

$$P_{geom}\% = \left(1 - \frac{V_{struts}}{V_{tot}}\right) \times 100 \quad \text{(Eq.4)}$$

The bulk density was calculated as the mass over volume ratio, whilst the true density was measured on crushed powders by He-Pycnomtery (UltraPyc 3000, Anton Paar). The porosity of the material was calculated as:

$$P_{mat}\% = \left(1 - \frac{\rho_{bulk}}{\rho_{true}}\right) \times 100 \quad \text{(Eq.5)}$$

The total porosity was calculated as:

$$P_{tot}\% = P_{geom} + P_{mat} \times V_{mat} \quad \text{(Eq.6)}$$

where P_{geom} and P_{mat} were calculated from equations (4) and (5), while V_{mat} was the volume occupied by struts over the total volume of the scaffolds.

XRD investigations were performed using a Bruker D8 Advance (Karlsruhe, Germany), Cu-ka radiation (λ = 1,541874 Å), 2θ = 10°–70°, step size 0.05. Morphological characterization was performed using FEG-SEM (Quanta-FEI Eindhoven, Netherland) equipped with an EDS probe (ThermoScientific, Ultradry) on samples after sintering.

Three-point bending tests were performed on 316L core filaments, on $CaTiSiO_5$ shell filaments so as on 316L- $CaTiSiO_5$ core-shell filaments (316L, P_{core} = 5 × 10^5 Pa) with a crosshead speed of 0.5 mm/min, on samples of useful length of 20 mm and diameter of approximately 1.4 mm using a Quasar 25, Galdabini S. p.a., Cardano al Campo, Italy. The flexural strength was calculated using Eqq. 7 and 8 for the dense filaments and shell filaments respectively:

$$\sigma_{br} = \frac{8FL}{\pi D^3} \quad \text{(Eq.7)}$$

$$\sigma_{br} = \frac{8FLD_0}{\pi\left(D_o^4 - D_i^4\right)} \quad \text{(Eq.8)}$$

where F is the applied force, D is the full filament diameter, D_0 and D_i are the outside (shell) and inside (core) filament diameter, and L is the filament length.

Compression tests were performed on sintered shell and core-shell scaffolds (316L_PEI, P_{core} = 5 × 10^5 Pa) with a crosshead speed of 0.5

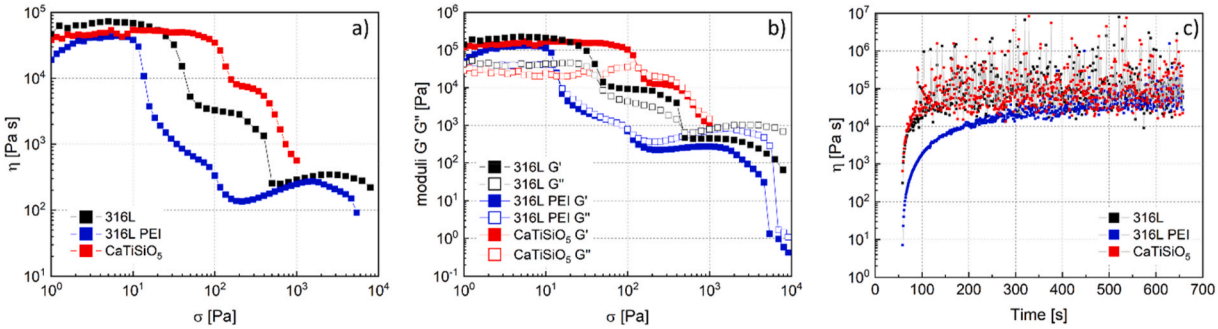

Fig. 4. Rheological behaviour of the three ink compositions: 316L, 316L_PEI and $CaTiSiO_5$.

Table 2
Rheological properties of the three testes inks.

Ink formulation	η_0 [Pa·s]	σ_y [Pa]	σ_F [Pa]	t_R [s]
316L	$6.4{\cdot}10^4$	16	474	101
316L_PEI	$3.9{\cdot}10^4$	11	14	6
$CaTiSiO_5$	$4.9{\cdot}10^4$	88	135	58

mm/min. All measurements were performed on at least 5 samples. We previously reported the compression test results of 316L scaffolds sintered at 1240 °C [19]. Compression strength was calculated as force over surface ratio. Measurements were performed on at least 5 samples. Weibull analysis was applied to calculate the characteristic load value so as the Weibull module under bending tests.

3. Results and discussion

3.1. Rheological characterization and printability

The rheological properties of core and shell inks are reported in Fig. 4 and Table 2. A slight decrease of zero -shear rate viscosity deriving from the addition of PEI as dispersant in 316L ink is clearly visible. Both core and shell inks exhibited the presence of a yield stress (Fig. 4b). After yield, 316L ink demonstrates a definite decay characterized by two slopes (marked slope from 10 to 20 Pa and gradual slope from 20 to 100 Pa) showing a double structure fluid. Rheological investigations on 316L ink previously reported [22], showed one single slope curve, where only distilled water was used in the binder composition. The two slopes are the result of different polymer-solvent interactions when both water and IPA are used. The LVR plateau, in $CaTiSiO_5$ ink, extends up to 100 Pa, and the high-volume ratio of sphene ink VR = 1.63 (316L ink, VR = 1.07) is the main reason for its high yield stress (Table 2), as previously shown [22]. A second plateau can be identified after yielding with a viscosity decreasing from 10^5 Pa·s to 10^4 Pa·s. Here, polysiloxane MK polymer, dissolved in IPA was used as a binder, and inorganic particles of various size distributions and compositions (SiO_2, $CaCO_3$ and TiO_2) were utilized to formulate the sphene ink. This behavior can be associated to a fluid capable of retaining part of its structure deriving from multiple particle-particle and particle-binder interactions. This is also reflected on recovery times (Fig. 4c) where for 316L ink $t_R > 100$ s, whilst for $CaTiSiO_5$ ink $t_R < 100$ s. The combination of high yield stress, low specific weight powders, and quick recovery durations observed for sphene ink allows to produce also empty shell structures capable of shape retention.

Filaments were printed using the parameters reported in Table 1. The core-shell filaments showed an under-extruded core, even when printed with maximum printing available pressure (5×10^5 Pa). To tune core size, PEI was added to the 316L ink, which had a clear effect on the ink's rheological properties as clearly visible in Fig. 4 and Table 2, with a reduction of zero shear stress viscosity, yield stress and the absence of the second plateau. The reduction of ink's strength could be appreciated

Sample	P [x10^5 Pa]	D_{core} [μm]	D_{shell} [μm]
316L_PEI-$CaTiSiO_5$	3	342±32	1754±80
	4	443±20	1755±50
	5	590±22	1376±53
316L-$CaTiSiO_5$	5	330±66	1279±19

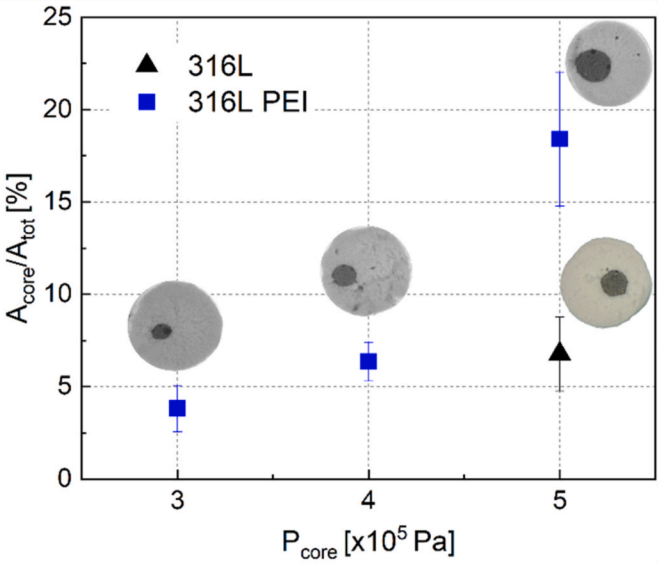

Fig. 5. Core area fraction of printed core-shell filaments at different pressures for 316L_PEI-$CaTiSiO_5$ and 316L-$CaTiSiO_5$. Core and shell average diameters and standard deviations after printing.

during the printing stage, where pressure could be varied from 3 to 5 (x10^5 Pa) with a clear effect on core size, as can be seen in Fig. 5. The core was positioned asymmetrically in the filament section, as shown in Fig. 5, and this can be attributed to the thin walls of the co-extrusion nozzle, which were easily displaced by the ink flow.

3.2. De-binding and sintering

The sintering process was designed following the results deriving from TGA-DTA analyses. As can be observed in Fig. 6 where 316L and $CaTiSiO_5$ inks derivative thermograms are reported, the 316L ink shows two main peaks at 250 °C and 390 °C corresponding to the PEG and PVA decomposition temperature, so as a weight increase starting at T > 600 °C that can be attributed to oxygen uptake from the chamber environment, during the measurement. $CaTiSiO_5$ exhibits significant weight losses across a wide temperature range, from 250 °C to 900 °C, due to MK crosslinking processes, solvent residues trapped within silicone chains, silicone-to-SiO_2 transformation, and lastly $CaCO_3$

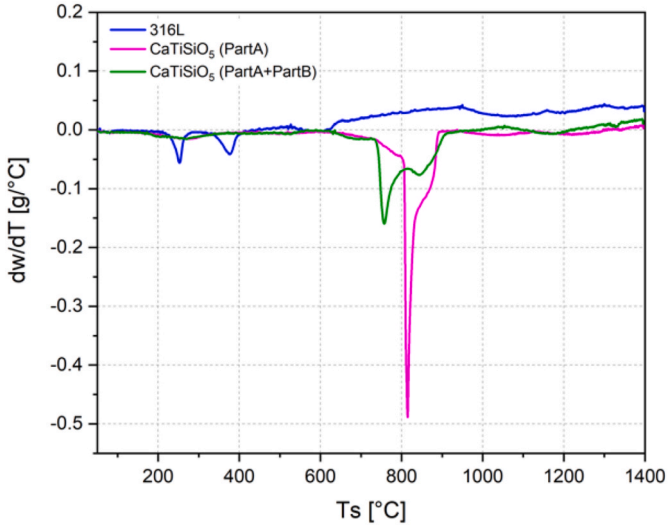

Fig. 6. TGA-DTA analyses of 316L ink, Sphene Ink PartA and core-shell 316L-Sphene (PartA + PartB), measurements were performed on dried extruded filaments.

degradation to CaO. $CaTiSiO_5$ shows a main peak at 810 °C followed by a shoulder extension that ends at 900 °C and corresponds to $CaCO_3$ decomposition. The 316L-$CaTiSiO_5$ inks show a broad peak (T = 200°C–300 °C) corresponding to PEG decomposition and MK crosslinking reactions, whilst the previous smaller peak attributed to PVA is not visible due to the small amount of steel present in the core-shell ink. The $CaCO_3$ decomposition begins at a lower temperature than the pure $CaTiSiO_5$ ink. This effect can be correlated to the presence of steel in the core-shell piece of filament used for the analysis, which alters thermal flow and diffusion, resulting in the temperature differential.

Mass loss and shrinkage were measured on scaffolds after drying and sintering. As can be observed from Table 3, measured mass losses are close to the calculated values for core-shell scaffolds, whilst higher values for shell scaffolds were measured. This discrepancy can be attributed to the presence of solvents that were not completely removed from the printed structures. The linear shrinkage is almost isotropic for $CaTiSiO_5$ scaffolds, the linear shrinkage for core-shell scaffolds on z-direction results higher than on x-y plane, due to the higher density of 316L ink. The volumetric shrinkage for the three compositions does not show a clear trend, with 316L-$CaTiSiO_5$ shrinking by 25.6% compared to 39.7% for 316LPEI-$CaTiSiO_5$. This result needs further investigations to be confirmed. After sintering, the scaffolds appeared to have a crack-free surface with porosity values reported in Table 3. Total porosity (P_{tot}) was higher than designed porosity (P_g) due to the intrinsic residual porosity deriving both from the core and shell parts, after the sintering process.

In Fig. 7, an example of core-shell 316L-$CaTiSiO_5$ scaffold is shown before (Fig. 7a and c) and after sintering (Fig. 7b and d) under the argon atmosphere. In addition, the surface of the scaffolds is also shown by stereo microscopy analysis (Fig. 7e and f) before and after sintering.

The printed scaffold geometry closely matches the designed

Table 3
Mass loss, linear and volumetric shrinkage of the scaffolds after the sintering process [Δm_{th} is the theoretical mass loss; Δm is the measured mass loss; ΔV is the volumetric shrinkage; P_d is the designed porosity; Pg is the geometrical porosity; P_{tot} is the total porosity].

Sample	Δm_{th} [%]	Δm [%]	ΔL_1 [%]	ΔL_2 [%]	ΔL_3 [%]	ΔV [%]	P_d [%]	P_g [%]	P_{tot} [%]
$CaTiSiO_5$	17.7	20.6 ± 0.45	14.2 ± 0.9	12.3 ± 0.5	13.5 ± 2.8	33.5 ± 0.9	64	55.0 ± 3	61.5 ± 3.7
316L- $CaTiSiO_5$	17.3	17.9 ± 2.0	9.2 ± 0.7	8.3 ± 0.6	11.5 ± 1.1	25.6 ± 2.5	59	52.0 ± 6.2	62.6 ± 2.0
316LPEI-$CaTiSiO_5$	16.2	16.1 ± 1.2	10.9 ± 0.7	9.9 ± 0.7	12.9 ± 1.2	39.7 ± 1.6	59	49.0 ± 7.3	66.8 ± 2.3

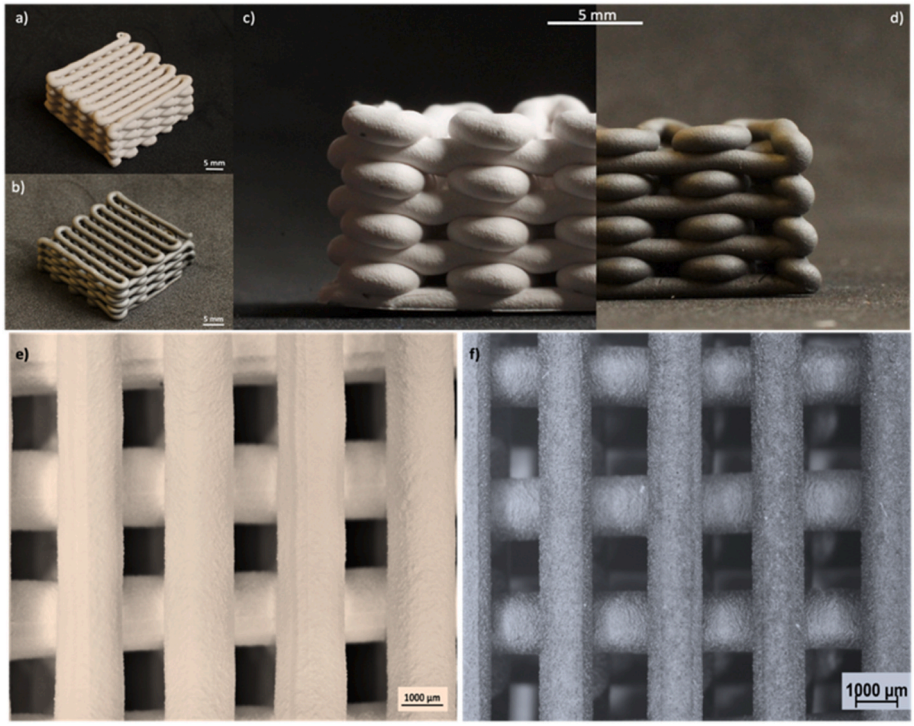

Fig. 7. 316L-$CaTiSiO_5$ core-shell scaffolds after printing (a, c, e) and after sintering (b, d, f) under Argon at 1240 °C.

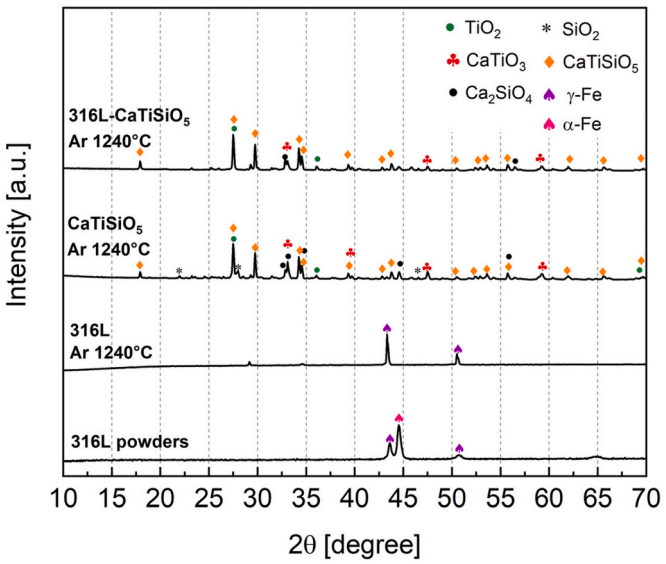

Fig. 8. XRD diffractograms of 316L powder as-received, 316L core, $CaTiSiO_5$ shell and 316L-$CaTiSiO_5$ core-shell filaments after sintering at 1240 °C under Argon flow.

geometry, even if a slight collapse of the structure can be observed on the span region. This effect is caused by the weight force of the ink and the ink yield strength [12].

The crystal structure of sintered samples was investigated using XRD analysis (Fig. 8). 316L starting powders are composed of α-Fe and γ-Fe, while only the austenitic γ phase was detected after sintering [28]. The shell $CaTiSiO_5$ sintered samples at 1240 °C show the presence of $CaTiSiO_5$ as the main crystal phase, besides $CaTiO_3$, $CaSiO_3$ and unreacted TiO_2 as secondary phases. The core-shell samples confirm the same composition, where iron was not detected. To understand the reason of this result, the microstructure of polished sections of sintered samples were analyzed by SEM coupled with EDS analysis (Figs. 9 and 10).

From Fig. 9a, it is possible to detect the presence of small pores (<10 μm) and of a Cr and Mo-rich second phase in 316L sintered filaments. In Fig. 9b where polished sections of sphene filaments are reported, it is possible to detect the presence of a main porous phase ($CaTiSiO_5$), as well as a second globular phase rich in Ti and Ca. A more precise analysis performed on the globular agglomerates is reported in [Figs. S3 and S4] where it is possible to detect the presence of a $Ca_xSi_yO_{x+y}$ envelope for $CaTiO_3$ and TiO_2 phases, corresponding to the detected peaks by XRD analysis. The porosity of $CaTiSiO_5$ can be ascribed to MK and $CaCO_3$ decomposition, whilst the globular second phase can be attributed to incomplete reaction and represents intermediate reaction products. In fact, the sphene is purely synthesized at T = 1300 °C in the air [17].

The core-shell crystal structure does not reveal the presence of g-Fe (Fig. 8) but mainly ceramic phases. In Fig. 10, it can be observed that the 316L-core experienced severe oxidation during the thermal treatment not only at the core-shell interface but also at the center of the core. From EDS analysis, a thick Cr and Mn-rich intergranular phase was formed on the surface of 316L particles, inhibiting their sintering with consequent structure embrittlement.

Despite the expectations, where an oxidation resistance steel was used so as an inert atmosphere, the synthesis environment seems to have played the main role in the Cr and Mn rich alloy. 316L stainless steel is well known for its oxidation resistance at medium temperatures (up to 600 °C) due to the formation of a Cr-rich corundum-type passivating oxide layer (Cr2-xFexO3). It was demonstrated [29] that at higher

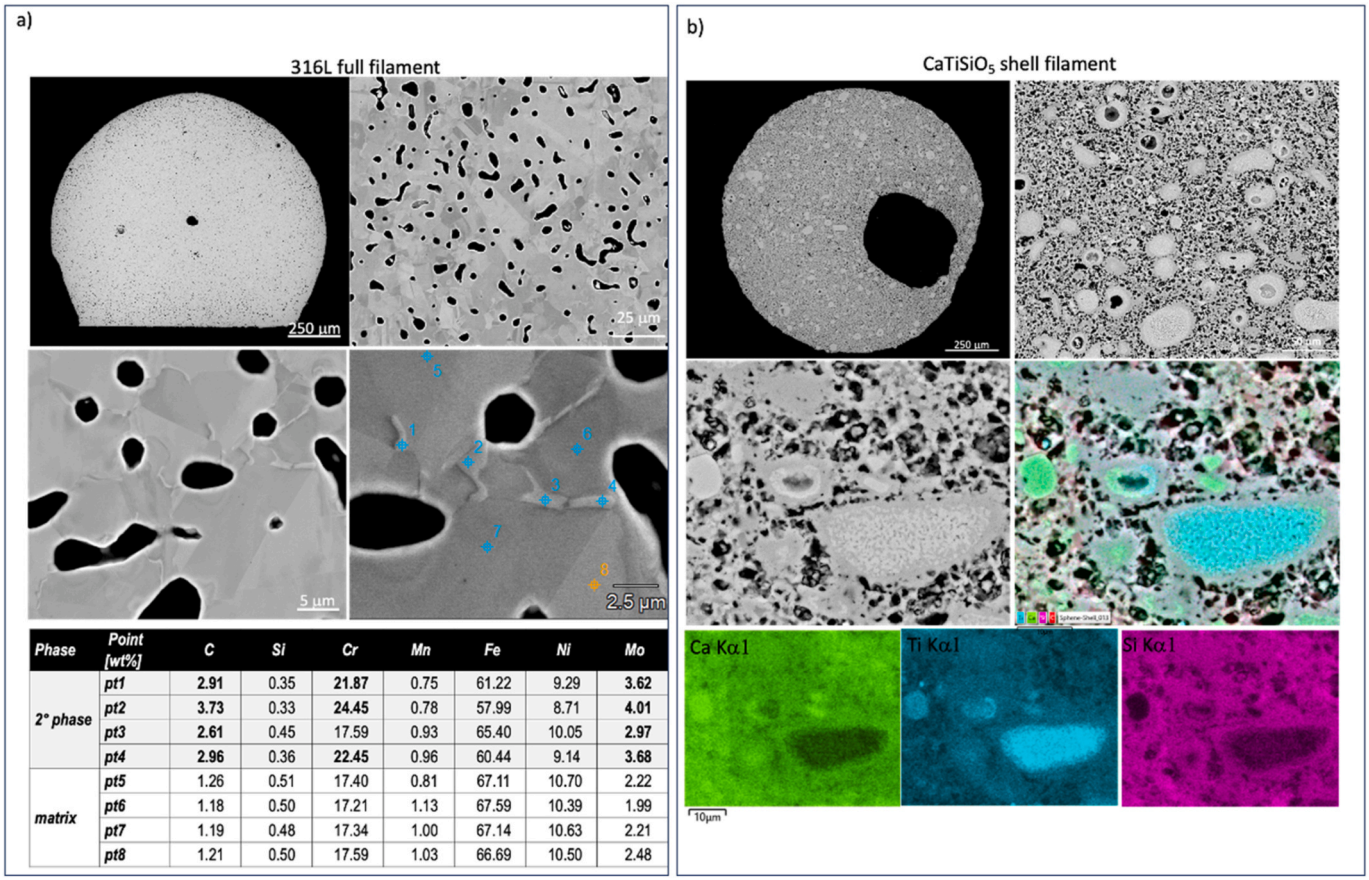

Phase	Point [wt%]	C	Si	Cr	Mn	Fe	Ni	Mo
2° phase	pt1	2.91	0.35	21.87	0.75	61.22	9.29	3.62
	pt2	3.73	0.33	24.45	0.78	57.99	8.71	4.01
	pt3	2.61	0.45	17.59	0.93	65.40	10.05	2.97
	pt4	2.96	0.36	22.45	0.96	60.44	9.14	3.68
matrix	pt5	1.26	0.51	17.40	0.81	67.11	10.70	2.22
	pt6	1.18	0.50	17.21	1.13	67.59	10.39	1.99
	pt7	1.19	0.48	17.34	1.00	67.14	10.63	2.21
	pt8	1.21	0.50	17.59	1.03	66.69	10.50	2.48

Fig. 9. SEM-EDS analysis of 316L (a) and $CaTiSiO_5$ (b) core and shell filaments respectively, after sintering at 1240 °C under Argon flow.

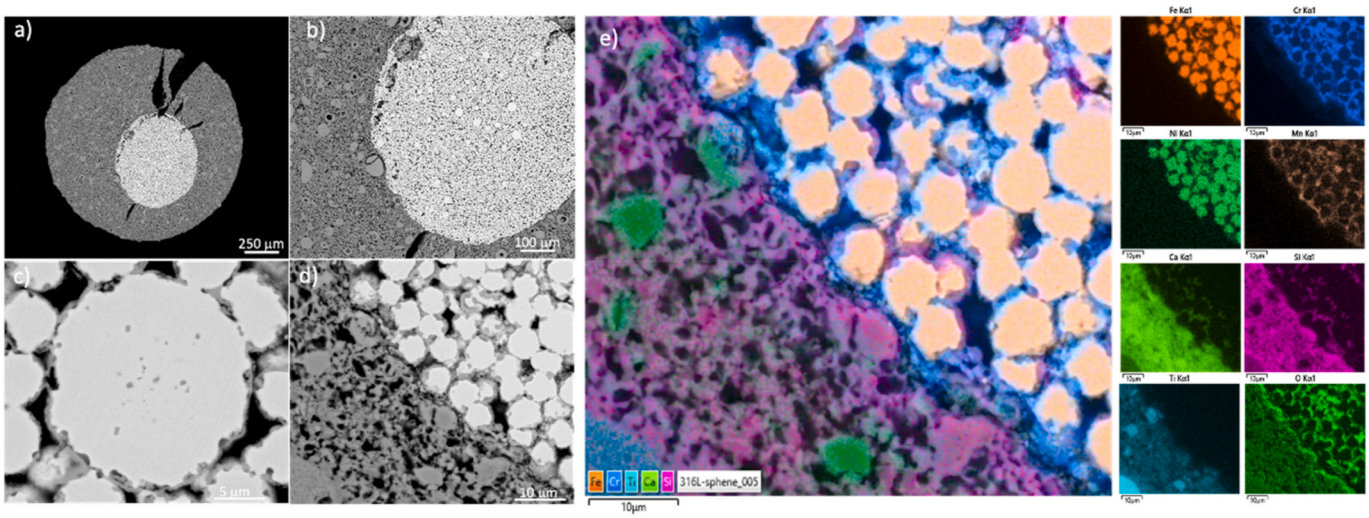

Fig. 10. SEM (a, b, c, d); and EDS (e) analysis of 316L-CaTiSiO$_5$ core-shell filaments respectively, after sintering at 1240 °C under argon flow.

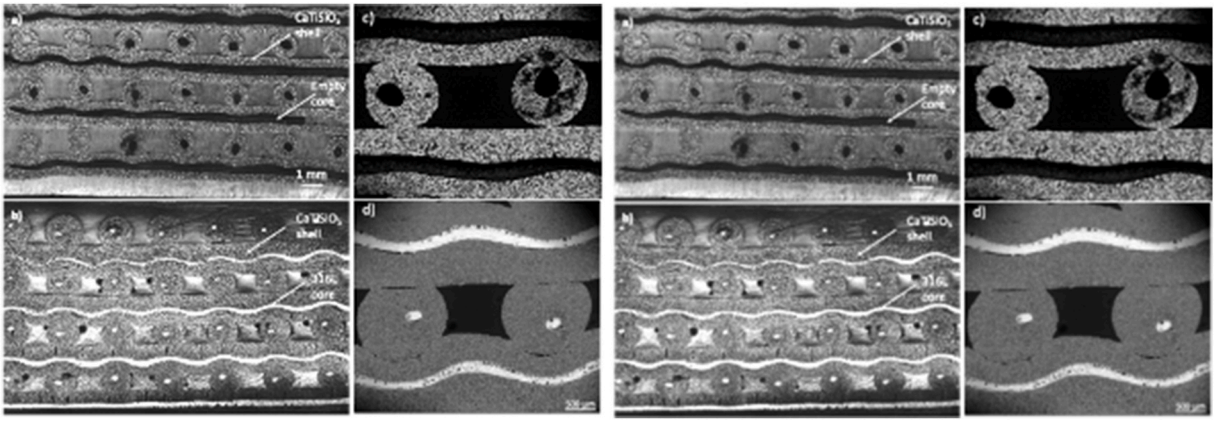

Fig. 11. SEM images of the shell (a,c) and core-shell ($P_{core} = 3 \times 10^5$ Pa) (b,d) scaffolds cross-sections after sintering.

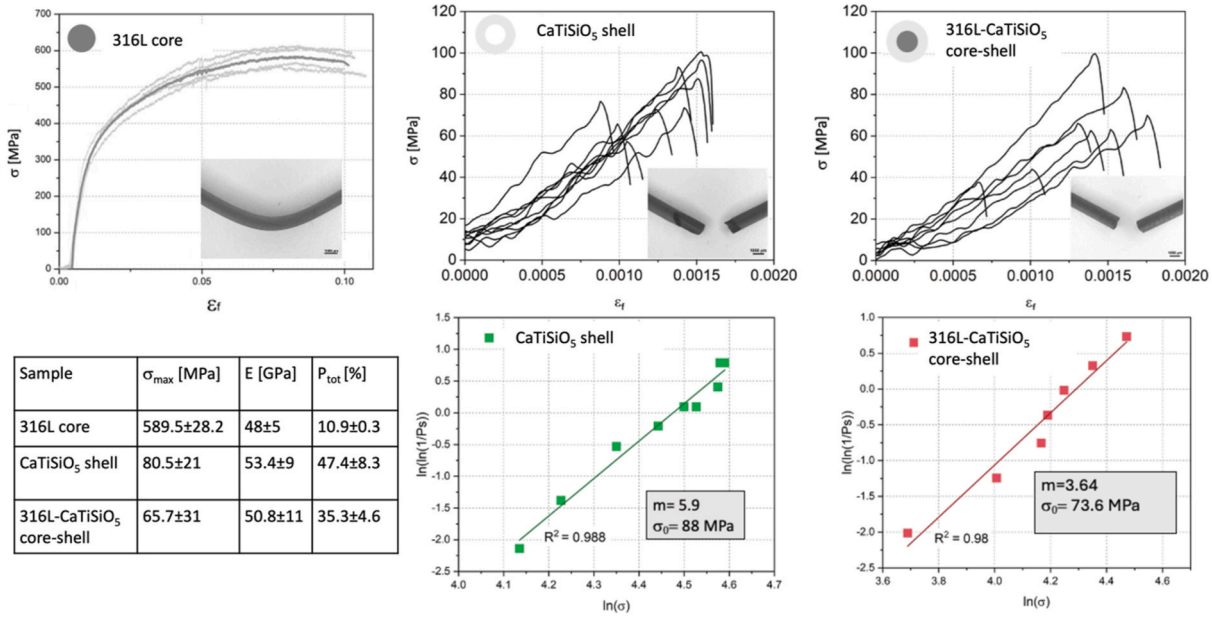

Sample	σ_{max} [MPa]	E [GPa]	P_{tot} [%]
316L core	589.5±28.2	48±5	10.9±0.3
CaTiSiO$_5$ shell	80.5±21	53.4±9	47.4±8.3
316L-CaTiSiO$_5$ core-shell	65.7±31	50.8±11	35.3±4.6

Fig. 12. 3-Points bending tests and Weibull analysis of core, shell and core-shell filaments (316L, $P_{core} = 3 \times 10^5$Pa).

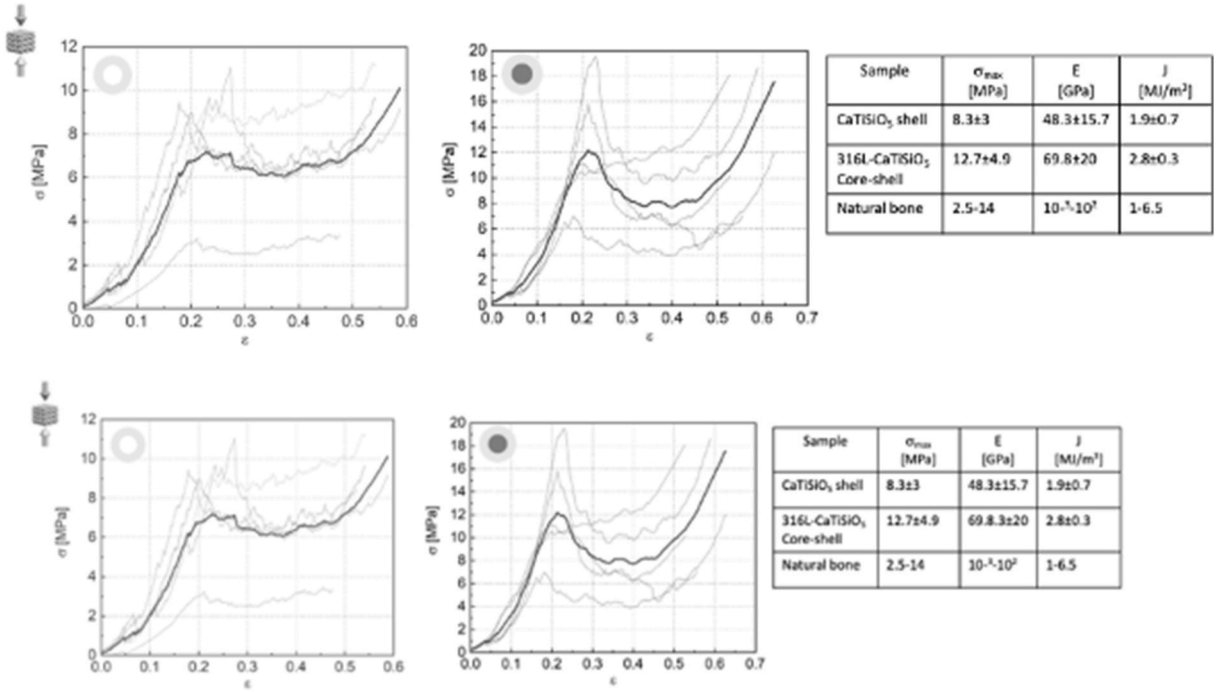

Sample	σ_{max} [MPa]	E [GPa]	J [MJ/m³]
$CaTiSiO_5$ shell	8.3±3	48.3±15.7	1.9±0.7
316L-$CaTiSiO_5$ Core-shell	12.7±4.9	69.8±20	2.8±0.3
Natural bone	2.5-14	10^{-3}-10^{2}	1-6.5

Sample	σ_{max} [MPa]	E [GPa]	J [MJ/m³]
$CaTiSiO_5$ shell	8.3±3	48.3±15.7	1.9±0.7
316L-$CaTiSiO_5$ Core-shell	12.7±4.9	69.8.3±20	2.8±0.3
Natural bone	2.5-14	10^{-3}-10^{2}	1-6.5

Fig. 13. Stress-strain curves under compression for shell and core-shell ($P_{core} = 5 \times 10^5$ Pa) scaffolds (left) and characteristic average values (table on the right).

temperatures (T = 800 °C in the air) the fraction of a non-protective spinel-type oxide is increased due to Mn diffusion. Even though CO_2 is a mild oxidative medium, its evolution during $CaCO_3$ decomposition may have favored the formation of the spinel-type oxides.

This is clearly visible in Fig. 10, where the core-shell section is reported. In Figs. 10a and 10b the whole section is reported with extensive radial crack formation. At higher magnifications, the 316L powders (Fig. 10c) show the presence of a thick oxide layer. In Figs. 10d and e the EDS map shows the concomitant presence of Cr and Mn at the grain boundaries, that in accordance to Ref. [29] can be associated to the formation of a non-protective spinel-type oxide.

Sections of embedded shell and core-shell scaffolds are reported in Fig. 11. The shell scaffolds display empty cores and a crack-free regular geometry (Fig. 11 a and c). The core-shell scaffolds (Fig. 11 b and d) show a regular geometry with 316L cores; however, the presence of radial cracks can be detected so as the presence of residual porosity on the core-shell interface in accordance with the porosity data reported in Table 3.

3.3. Mechanical properties

Three-point bending tests were performed on the sintered filaments, and results are reported in Fig. 12. The 316L core filament shows ductile behaviour, with a maximum strength of 589 MPa, this value is in good agreement with literature data and in accordance with the measured porosity of 10.9%. The Young modulus results were lower than expected and the samples did not reach failure during the test. The $CaTiSiO_5$ filaments showed a clear brittle behaviour with a maximum strength of 80.5 MPa and E = 53.4 GPa. Weibull analysis performed on a limited number of samples shows a Weibull modulus of m = 5.9 and the value of characteristic strength equal to 88 MPa. The core-shell filaments also showed brittle behaviour due to the extensive oxide formation within

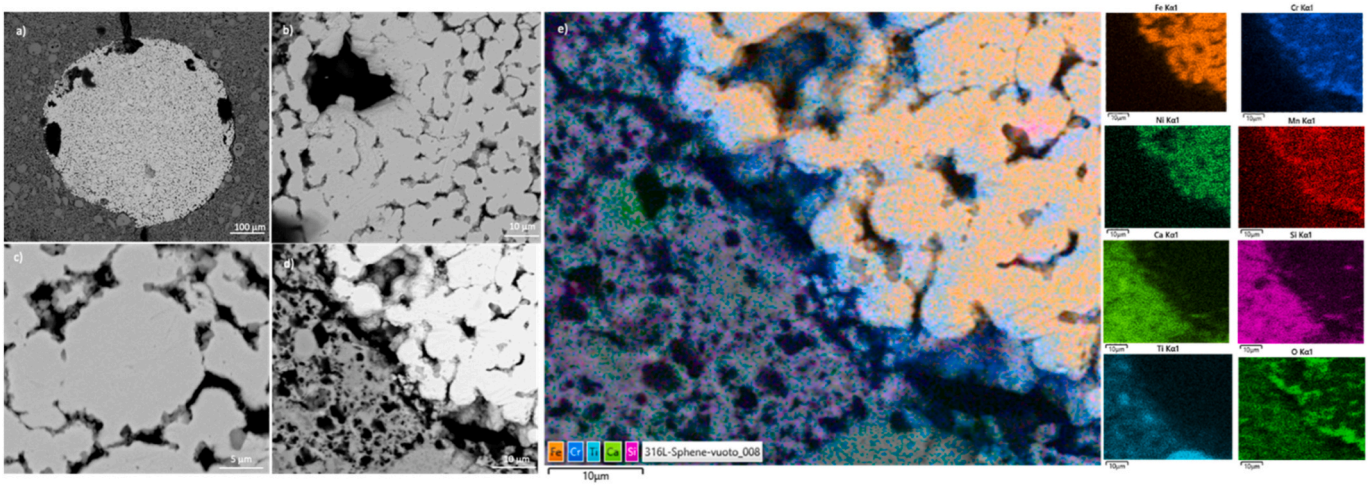

Fig. 14. SEM (a, b, c, d) and EDS (e) analysis of 316L-$CaTiSiO_5$ core-hell scaffold, after sintering at 1240 °C under argon flow and applied vacuum in the range 700°C–900 °C.

the core 316L particles, with high values of porosity (P_{tot} = 35%), and maximum strength and Weibull parameters slightly lower than those observed in shell filaments. Bending tests on core-shell filaments could be performed only on 316L ink composition, since the core-shell filaments with core 316L_PEI, extruded at $P_{core} = 5 \times 10^5$ Pa showed severe crack formation upon sintering.

Compression strength tests reported in Fig. 13 were performed on shell and core-shell scaffolds. The shell scaffolds show compression strength values typical for highly porous structures. Despite the brittle behaviour of core-shell structures as a consequence of inhibited sintering and oxide formation, their compression strength (σ_{max}), Young's modulus (E), and strain energy density (MJ/m^3) resulted in higher average values than the shell structures (table in Fig. 13).

However, the shell and core-shell scaffolds exhibit similar overall porosity, as demonstrated in Table 3. We can see that the core-shell scaffolds had better mechanical properties compared to the shell-scaffolds. In particular, the compressive strength of the core-shell scaffolds significantly increased by approximately 53% (from σ_{max} = 8.3 MPa to from σ_{max} = 12.7 MPa) compared to the shell structures. All strength values were close to the maximum cancellous bone range strength [7,30,31].

To confirm the hypothesis of CO_2 oxidation, one core-shell scaffold was heat treated by applying mild vacuum (0.1–1 Pa) in the 700°C–900 °C temperature range (following TGA-DTA results reported in Fig. 6) and argon flow, using the thermal cycle reported in the experimental section.

SEM-EDS analyses were performed on the polished section of the embedded sample. As can be observed from Fig. 14, the Cr and Mn diffusion at the 316L steel grain boundaries is inhibited thus reducing the amount of intergranular spinel-type oxide formation. Despite the encouraging result, the mild vacuum applied was insufficient to prevent the 316L oxidation, with consequent embrittlement of the structure.

4. Conclusions

In this paper, we report on the feasibility of a one-step co-extrusion process to produce shell and core-shell structures characterized by an in situ synthesized bio-ceramic shell and a 316L core. The printability was demonstrated by employing proper ink formulations and co-extrusion nozzle design. Sphene shell structures were sintered by reactive sintering and showed shape retention with struts characterized by empty cores. The hierarchical porosity deriving from the 3D structure, empty cores and struts make this structure particularly interesting for bone replacement applications. The de-binding and sintering steps showed a negative effect for the core-shell structures where the CO_2 emission, deriving from $CaCO_3$ decomposition used as Ca precursor for sphene formation, catalyzed the formation of a non-protective spinel oxide among the 316L particles thus inhibiting sintering and consequent embrittlement. The compression strength of the produced scaffolds showed values compatible with the requested values as bone-substitutes, so as an improvement of both compression strength and strain energy density compared to the shell ceramic scaffolds. Further work is ongoing to inhibit the formation of the oxide layers, therefore various sphene precursors and core materials will be examined. Overall, the present work offers a methodology to co-extrude diverse materials in one step and represents a starting point for further investigations with different combinations of metal-ceramics and metal-metal structures. The understanding and modeling of the role of core size over the shell size, core-shell interfacial strength, and thermally induced stress still represent open points that need dedicated work.

Data availability

Data will be made available on request.

Funding

This work represents the first results of Multi-functional 3D printed bio-scaffolds, MULTIFUN3D PROJECT #2022T4LPER, funded by MUR and EU– Next Generation EU.

Declaration of competing interest

The authors declare the following financial interests/personal relationships which may be considered as potential competing interests: Lisa Biasetto reports financial support was provided by Italian Ministry of University and Research-MUR. Lisa Biasetto reports financial support was provided by European Union. If there are other authors, they declare that they have no known competing financial interests or personal relationships that could have appeared to influence the work reported in this paper.

Acknowledgments

Alberto Fabrizi (Department of Management and Engineering, university of Padova) for performing part of EDS analysis, and Giorgia Franchin (Department of Industrial Engineering, University of Padova) and Michele Lollo (LNL-INFN) for kind support with co-extrusion nozzle design and production.

Appendix A. Supplementary data

Supplementary data to this article can be found online at https://doi.org/10.1016/j.jmrt.2024.10.255.

References

[1] Mueller J, Raney JR, Shea K, Lewis JA. Architected lattices with high stiffness and toughness via multicore–shell 3D printing. Adv Mater 2018;30:1705001. https://doi.org/10.1002/adma.201705001.
[2] Wang P, Sun Y, Li D, Ma Z, Zhang B, Diao L, Liu H. Extrusion-based 3D co-printing: printing material design and novel workflow for fabricating patterned heterogeneous tissue structures. Mater Des 2023;227:111737. https://doi.org/10.1016/j.matdes.2023.111737.
[3] Zhou W, Li X, Duan H, Lv P. Multi-material integrated three- dimensional printing of cylindrical Li-ion battery. J Manuf Sci Eng 2022;144. https://doi.org/10.1115/1.4052707. 064501-064501.
[4] Yang Z, Jia S, Niu Y, Lv X, Fu H, Zhang Y, Liu D, Wang B, Li Q. Bean-pod-inspired 3D-printed phase change microlattices for solar-thermal energy harvesting and storage. Small 2021;17:2101093. https://doi.org/10.1002/smll.202101093.
[5] Fu Z, Freihart M, Schlordt T, Fey T, Kraft T, Greil P, Travitzky N. Robocasting of carbon-alumina core-shell composites using co-extrusion. Rapid Prototyp J 2017; 23:423–33. https://doi.org/10.1108/RPJ-12-2015-0191.
[6] Zhou S, Cai Q, Tirichenko IS, Vilchez V, Gavalda-Diaz O, Bouville F, Saiz E. Additive manufacturing of Al2O3 with engineered interlayers and high toughness through multi-material co-extrusion. Acta Mater 2023;246:118704. https://doi.org/10.1016/j.actamat.2023.118704.
[7] Paredes C, Martínez-Vázquez FJ, Pajares A, Miranda P. Novel strategy for toughening robocast bioceramic scaffolds using polymeric T cores. Ceram Int 2019; 45:19572–6. https://doi.org/10.1016/j.ceramint.2019.06.175.
[8] Cipollone D, Mena JA, Sabolsky K, Sabolsky EM, Sierros KA. Coaxial ceramic direct ink writing on heterogenous and rough surfaces: investigation of core-shell interactions. ACS Appl Mater Interfaces 2022;14:24897–907. https://doi.org/10.1021/acsami.2c03250.
[9] Moreno-Sanabria L, Ramírez C, Osendi MI, Belmonte M, Miranzo P. Thermal conductivity of three-dimensional multi-material core-shell filament structures obtained by material extrusion. Addit Manuf 2024;81:104018. https://doi.org/10.1016/j.addma.2024.104018.
[10] Cai Q, Meille S, Chevalier J, Zhou S, Bouville F, Tirichenko I, Saiz E. 3D-printing of ceramic filaments with ductile metallic cores. Mater Des 2023;225:111463. https://doi.org/10.1016/j.matdes.2022.111463.
[11] Wei P, Cipriani C, Hsieh C-M, Kamani K, Rogers S, Pentzer E. Go with the flow: rheological requirements for direct ink write printability. J Appl Phys 2023;134: 100701. https://doi.org/10.1063/5.0155896.
[12] M'Barki A, Bocquet L, Stevenson A. Linking rheology and printability for dense and strong ceramics by direct ink writing. Sci Rep 2017;7:6017. https://doi.org/10.1038/s41598-017-06115-0.
[13] Selsing J. Internal stresses in ceramics. J Am Ceram Soc 1961;8:419. https://doi.org/10.1111/j.1151-2916.1961.tb15475.x.
[14] Wang L, Qi Q, Wu H, Zhang H, Yin J, Yang Y, Huang J, Yang X, Liu X, Huang Z. Stress distribution around Fe5Si3 and its effect on interface status and mechanical

properties of Si3N4 ceramics. J Am Ceram Soc 2018;101:856–64. https://doi.org/10.1111/jace.15240.
[15] Wang L, Qi Q, Yang X, Zhang H, Liu Z, Ge S, Peng X, Liu L, Liu Y, Liu X, Huang Z, Jiang D. Mechanical properties optimization of Si3N4 ceramics by in-situ introduction of core-shell structural W-Fe5Si3. Comp. Part B: Engineering 2020; 196:108134. https://doi.org/10.1016/j.compositesb.2020.108134.
[16] Brunello G, Biasetto L, Elsayed H, Sbettega E, Gardin C, Scanu A, Carmignato S, Zavan B, Sivolella S. An in vivo study in rat femurs of bioactive silicate coatings on titanium dental implants. J Clin Med 2020;9:1290. https://doi.org/10.3390/jcm9051290.
[17] Elsayed H, Sayed M, Naga SM, Rebesan P, Gardin C, Zavan B, Colombo P, Bernardo E. Additive manufacturing and direct synthesis of sphene ceramic scaffolds from a silicone resin and reactive fillers. J Eur Ceram Soc 2022;42: 286–95. https://doi.org/10.1016/j.jeurceramsoc.2021.10.001e.
[18] Brunello G. Bioactive sphene coatings for dental implant applications. 2020. PhD Thesis.
[19] Biasetto L, Elsayed H. Direct ink writing of AISI 316L dense parts and porous lattices. Adv. Mat Eng. 2022;24:2101729. https://doi.org/10.1002/adem.202101729.
[20] Elsayed H, Rebesan P, Giacomello G, Pasetto M, Gardin C, Ferroni L, Zavan B, Biasetto L. Direct ink writing of porous titanium (Ti6Al4V) lattice structures. Mater Sci Eng C 2019;103:109794. https://doi.org/10.1016/j.msec.2019.109794.
[21] Elsayed H, Brunello G, Gardin C, Ferroni L, Badocco D, Pastore P, Sivolella S, Zavan B, Biasetto L. Bioactive sphene-based ceramic coatings on cpTi substrates for dental implants: an in vitro study. Materials 2018;11:2234. https://doi.org/10.3390/ma11112234.
[22] Biasetto L, Gleadall A, Gastaldi V. Ink tuning for direct ink writing of planar metallic lattices. Adv Eng Mater 2023;25:2201858. https://doi.org/10.1002/adem.202201858.
[23] Christopher J, Dimitriou, Ewoldt Randy H, McKinley Gareth H, Rheol J, editors. Describing and prescribing the constitutive response of yield stress fluids using large amplitude oscillatory shear stress (LAOStress); 2013. p. 27. https://doi.org/10.1122/1.4754023. 57.
[24] Rocha VG, Saiz E, Tirichenko IS, Garcia- Tunon E. Direct ink writing advances in multi-material structures for a sustainable future. J Mater Chem A 2020;8:15646. https://doi.org/10.1039/D0TA04181E.
[25] Morrison FA. Understanding rheology. Oxford University Press; 2001.
[26] Gleadall A. FullControl GCode Designer: open-source software for unconstrained design in additive manufacturing, vol. 46; 2021, 102109. https://doi.org/10.1016/j.addma.2021.102109.
[27] Biasetto L, Elsayed H. Direct ink writing of AISI 316L dense parts and porous lattices. Adv. Mat Eng. 2022;24:2101729. https://doi.org/10.1002/adem.202101729.
[28] Puscas TM, Molinari A, Kazior J, Pieczonka T, Nykiel M. Sintering Transformations in mixtures of austenitic and ferritic stainless steel powders. Powder Metall 2001; 44:48–52. https://doi.org/10.1179/003258901666167.
[29] Wonneberger R, Lippmann S, Abendroth B, Carlsson A, Seyring M, Rettenmayr M, Undisz A. Bridging the gap between high temperature and low temperature oxidation T of 316 L. Corrosion Sci 2020;175:108884. https://doi.org/10.1016/j.corsci.2020.108884.
[30] Jones JR, Ehrenfried LM, Hench LL. Optimising bioactive glass scaffolds for bone tissue engineering. Biomaterials 2006;27:964–73. https://doi.org/10.1016/j.biomaterials.2005.07.017.
[31] Gerhardt L-C, Boccaccini AR. Bioactive glass and glass-ceramic scaffolds for bone tissue engineering. Materials 2010;3:3867–910. https://doi.org/10.3390/ma3073867.